VHF Free–Free Beam High-Q Micromechanical Resonators

Kun Wang, *Member, IEEE*, Ark-Chew Wong, *Student Member, IEEE*, and Clark T.-C. Nguyen, *Member, IEEE*

***Abstract*—Free–free-beam flexural-mode micromechanical resonators utilizing nonintrusive supports to achieve measured Qs as high as 8400 at VHF frequencies from 30 to 90 MHz are demonstrated in a polysilicon surface micromachining technology. The microresonators feature torsional-mode support springs that effectively isolate the resonator beam from its anchors via quarter-wavelength impedance transformations, minimizing anchor dissipation and allowing these resonators to achieve high-Q with high stiffness in the VHF frequency range. The free–free-beam micromechanical resonators of this paper are shown to have an order of magnitude higher Q than clamped–clamped-beam versions with comparable stiffnesses. [499]**

***Index Terms*—Anchor loss, electromechanical coupling, IF filter, MEMS, microelectromechanical devices, motional resistance, quality factor, resonator, VHF.**

NOMENCLATURE

A	Transmission gain measured on a network analyzer.
C_∞	Measurement circuit bias-tee capacitor.
h	Resonator beam thickness.
$d(y)$	Electrode-to-resonator gap spacing at location y along the resonator beam length.
$d_{\rm ini}$	Initial electrode-to-resonator gap spacing before pull-down.
E	Young's modulus of elasticity.
ε_o	Permittivity in vacuum (= 8.854×10^{-12} F/m).
$f_{\rm nom}$	Resonance frequency of a mechanical resonator with no electromechanical coupling.
f_o	Resonance frequency of a mechanical resonator including electromechanical coupling.
G	Shear modulus of elasticity.
γ	Torsion constant.
I_r	Bending moment of inertia (resonator beam).
i_z	Motional current.
I_z	Motional current magnitude.
J_s	Polar moment of inertia (support beam).
κ	Shear-deflection coefficient.
k_e	Electrical stiffness arising from electromechanical coupling.
$KE_{\rm tot}$	Peak total kinetic energy.
$\langle k_e/k_m \rangle$	Electrical-to-mechanical stiffness ratio integrated over the electrode width.
$k_r(y)$	z-direction equivalent stiffness of a resonator beam at location y along its length.
$k_m(y)$	z-direction mechanical stiffness at location y of a resonator beam with $V_P = 0$ V.
k_s	Combined z-direction stiffness of all supporting beams.
L_1	Lower electrode edge location.
L_2	Upper electrode edge location.
L_P	Measurement circuit bias-tee inductor.
L_r	Resonator beam length.
L_s	Support beam length.
$m_r(y)$	Equivalent mass of a resonator beam at location y along its length.
ν	Poisson's ratio.
ρ	Density.
Q	Unloaded quality factor.
Q_l	Loaded quality factor.
$R_{\rm amp}$	Transresistance amplifier gain.
R_L	Measurement load resistance.
R_p	Parasitic interconnect resistance.
R_x	x-direction series motional resistance.
R_z	z-direction series motional resistance.
v_i	Input voltage.
V_i	Input voltage magnitude.
$v(y)$	Velocity at location y of a resonator beam.
V_c	Catastrophic pull-in voltage.
V_d	Dimple-down pull-in voltage.
V_P	Resonator dc-bias voltage.
v_o	Output voltage developed across R_L.
$\omega_{\rm nom}$	$f_{\rm nom}$ in radians/seconds.
ω_o	f_o in radians/seconds.
W_e	Electrode width.
W_r	Resonator beam width.
W_s	Support beam width.
ζ	Frequency modification fitting factor.
$Z_{\rm mode}(y)$	Mode shape function.

Manuscript received October 18, 1999; revised May 29, 2000. This work was supported by the Defense Advanced Research Projects Agency under Agreement F30602-97-2-0101, by the National Science Foundation, and by the National Aeronautics and Space Administration/Jet Propulsion Laboratory. Subject Editor, G. Stemme.

K. Wang was with the Department of Electrical Engineering and Computer Science, The University of Michigan at Ann Arbor, Ann Arbor, MI 48109-2122 USA. He is now with Delphi Research and Development, Delphi Automotive Systems, Warren, MI 48090-9055 USA.

A.-C. Wong and C. T.-C. Nguyen are with the Department of Electrical Engineering and Computer Science, The University of Michigan at Ann Arbor, Ann Arbor, MI 48109-2122 USA.

Publisher Item Identifier S 1057-7157(00)08025-2.

I. INTRODUCTION

VIBRATING beam micromechanical (or "μmechanical") resonators constructed in a variety of materials, from poly-crystalline silicon to plated-nickel, have recently emerged

1057–7157/00$10.00 © 2000 IEEE

as potential candidates for use in a variety of frequency-selective communications applications [1]. In particular, provided the needed VHF and UHF ranges can be attained, both low loss IF and RF filters and high-Q oscillators stand to benefit from the tiny size, virtually zero dc power consumption, and integrability of such devices. To be useful for direct insertion into present-day cellular and cordless phone applications, μmechanical resonators used in IF filters must be capable of operating at frequencies from 70 to 250 MHz, while those aimed at RF filters must attain a range from 800 MHz to 1.8 GHz.

To date, due to the relative ease with which they attain large stiffness-to-mass ratios, clamped–clamped beam μmechanical resonators have been intensively investigated for VHF range applications [2]–[4]. The ability to simultaneously achieve high-Q and high stiffness is paramount for *capacitively driven* communications-grade resonators since stiffness directly influences the dynamic range of circuits comprised of such resonators [5], [6]. In particular, for a flexural mode μmechanical resonator using a parallel-plate capacitive transducer, the higher the stiffness, the higher the dynamic range for the common case where third-order intermodulation distortion dominates. The reasons for this are detailed more extensively in [5] and [6], but a heuristic understanding arises from the recognition that VHF range flexural-mode beams with lengths from 10 to 30 μm and electrode-to-resonator gap spacings from 400 to 1000 Å, typically operate with peak displacements on the order of only 10–20 Å. At these amplitudes, capacitive (rather than material) nonlinearity is responsible for generation of third-order intermodulation distortion. Thus, for a given electrode-to-resonator gap spacing, distortion can be reduced by increasing the beam stiffness since this reduces the displacement amplitudes caused by out-of-band (off-resonance) interferers faster than it does the in-band electrical output level (when capacitive transduction is utilized).

However, for the case of clamped–clamped beam designs, larger stiffness often comes at the cost of increased anchor dissipation and, thus, lower resonator Q. Thus, to date, the highest Qs (~20 000) for VHF μmechanical resonators have been achieved using submicrometer technologies to scale dimensions (and masses) down to the point where the required stiffnesses are small [3]. Unfortunately, although their Qs are impressive, the stiffnesses of these resonators are too small to achieve adequate dynamic range and power-handling ability for most communications applications, where large adjacent channel interferers must often be suppressed.

This paper attempts to address the above problems by retaining the basic flexural-mode beam design of previous resonators, but strategically altering their supports so that anchors and their associated losses are virtually eliminated from the design. With anchor losses suppressed, high-stiffness VHF resonator beams can now be utilized, with dynamic ranges more applicable to communications applications. Using this approach, free–free beam μmechanical resonators are demonstrated with center frequencies from 30 to 90 MHz, stiffnesses from 30 000 to 80 000 N/m, and Qs as high as 8400.

This paper begins with a general description of free–free beam μmechanical structure and operation in Section II, followed by design details in Section III. Fabrication and experimental results then follow in Sections IV and V, respectively. The paper then concludes with brief comments on the ultimate frequency range of this free–free beam design.

II. Resonator Structure and Operation

Fig. 1 presents several schematics describing the free–free beam μresonator of this paper, including a perspective view indicating key features and specifying a preferred electrical readout scheme, an overhead layout view identifying key dimensions, and a mode shape schematic generated via finite-element simulation. As shown, this device is comprised of a free–free μmechanical beam supported at its flexural node points by four torsional beams, each of which is anchored to the substrate by rigid contact anchors. An electrode is provided underneath the free–free beam to allow electrostatic excitation via an applied ac voltage v_i. The electrical operation of this structure is very similar to that of previous clamped–clamped beam resonators [6]–[9], in that a dc-bias voltage V_P applied to the resonator structure is required to amplify v_i-derived force components at the frequency of v_i, and the detected output current i_{zo} is generated by the action of V_P across the time-varying (at resonance) electrode-to-resonator capacitor $C(z,t)$: $i_{zo} = V_P(\partial C/\partial t)$. Note that, unlike many of its two-port predecessors, this device is a one-port device, so its output current must be taken directly off the resonator structure [9]. To allow sensing of the output current i_{zo} from the resonator structure while also applying the dc-bias V_P, a bias tee consisting of the inductor L_P and coupling capacitor C_∞ is utilized. R_L represents the load presented by the measurement instrument—most often the 50 Ω seen into the sense port of a network analyzer.

The torsional support beams for this device are strategically designed with quarter-wavelength dimensions, so as to affect an impedance transformation that isolates the free–free beam from the rigid anchors. Ideally, the free–free beam sees zero-impedance into its supports and, thus, effectively operates as if levitated without any supports. As a result, anchor dissipation mechanisms found in previous clamped–clamped beam resonators are greatly suppressed, allowing much higher device Q.

As an additional yield-and Q-enhancing feature, the transducer capacitor gap spacing in this device is no longer entirely determined via a thin sacrificial oxide, as was done (with difficulty) in previous clamped–clamped beam high-frequency devices [1], [4]. Rather, the capacitor gap is now determined by the height of a dimple, set via a timed etch. As shown in Fig. 2, the height of the dimple is such that when a sufficiently large dc-bias V_P is applied between the electrode and resonator, the whole structure comes down and rests upon the dimples, which are located at flexural node points and, thus, ideally have little impact on resonator operation. The advantages of using dimples to set the capacitor gap spacings are twofold: 1) much thicker sacrificial oxide spacers can now be used, alleviating previous problems due to pinholes and nonuniformity in ultra-thin sacrificial layers and 2) the thicker sacrificial oxide is easier to remove than

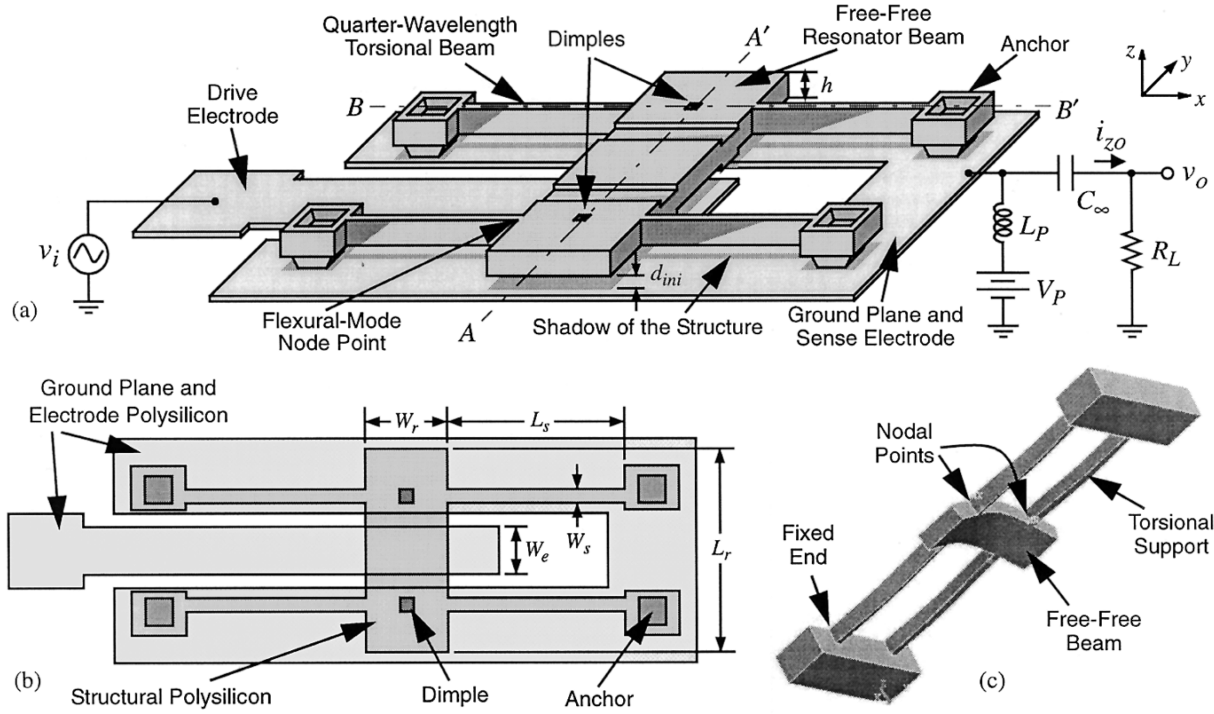

Fig. 1. (a) Perspective view schematic of the free–free beam resonator with nonintrusive supports, explicitly indicating important features and specifying a typical bias, excitation, and off-chip output sensing configuration. (b) Overhead layout view, indicating dimensions to be used in later analyses. (c) The mode shape of the resonator obtained via finite-element simulation using ANSYS.

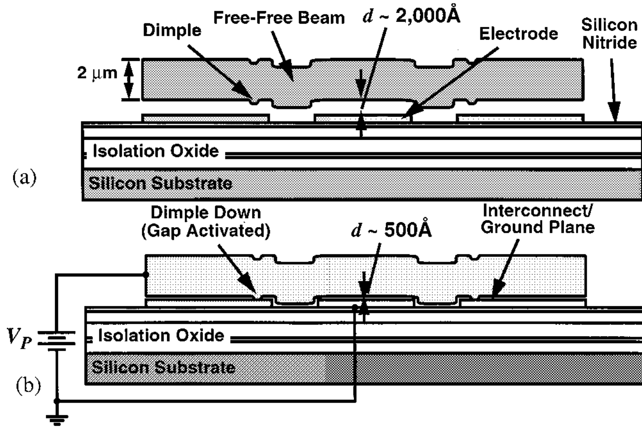

Fig. 2. Cross sections (along AA' in Fig. 1) summarizing the electrostatically activated capacitor gap feature of this design. (a) Immediately after fabrication. (b) After application of an appropriately sized dc-bias voltage $V_P > V_d$.

previous thinner ones and, thus, decreases the required HF release etch time and lessens the chance that etch byproducts remain in the gap (where they might interfere with resonator operation and Q [1], [4]).

III. Free–Free Beam Microresonator Design

Proper design of the free–free beam μmechanical resonator entails not only the selection of geometries that yield a given frequency, but also geometries that insure support isolation that guarantee the beam does not pull into the electrode once pulled down on its dimples by V_P, and that suppress spurious modes associated with the more complicated support network. Each of these topics is now addressed.

A. Resonance Frequency Design for an Uncoupled Beam: Euler–Bernoulli Versus Timoshenko Methods

For most practical designs, the resonator beam width W_r is governed by transducer and length-to-width ratio design considerations, while its thickness h is determined primarily by process constraints. Almost by default then, the length L_r becomes the main variable with which to set the overall resonance frequency. For the case of large L_r-to-W_r and L_r-to-h ratios, the popular Euler–Bernoulli equation for the fundamental mode frequency of a free–free beam suffices. For a narrow free–free or clamped–clamped beam with uniform cross section in the absence of electromechanical coupling, the Euler–Bernoulli equation for resonance frequency in the z-direction is [12]

$$f_{\text{nom}} = 1.03\sqrt{\frac{E}{\rho}}\,\frac{h}{L_r^2} \tag{1}$$

where E and ρ are the Young's modulus and density of the structural material, respectively, and h and L_r are indicated in Fig. 1.

Equation (1) constitutes a convenient closed-form relation that works well for low-frequency designs, where beam lengths are much larger than their thicknesses. For upper VHF designs, for which beam lengths begin to approach their thickness dimensions, the Euler–Bernoulli equation is no longer accurate since it ignores shear displacements and rotary inertias. To obtain accurate beam lengths for upper VHF μmechanical resonators, the design procedure by Timoshenko is more appropriate [13], involving the simultaneous solution of the coupled equations

$$\frac{\partial}{\partial y}\left(EI_r\frac{\partial \psi}{\partial y}\right) + \kappa h W_r G\left(\frac{\partial z}{\partial y} - \psi\right) - \rho I_r \frac{\partial^2 \psi}{\partial t^2} = 0 \tag{2}$$

$$\rho\frac{\partial^2 z}{\partial t^2} - \frac{\partial}{\partial y}\left[\kappa G\left(\frac{\partial z}{\partial y} - \psi\right)\right] = 0 \quad (3)$$

where

$$I_r = \frac{W_r h^3}{12} \quad \text{and} \quad G = \frac{E}{2(1+\nu)} \quad (4)$$

and where I_r is the bending moment of inertia, G is the shear modulus of elasticity, ν is Poisson's ratio, κ is the shear-deflection coefficient (for a rectangular cross section, κ is 2/3), ψ is the slope due to bending, and axis definitions are provided in Fig. 1.

For a free–free beam with uniform cross section, again, sans any electromechanical coupling, (2)–(4) yield the following equation that can be solved for the fundamental resonance frequency ω_{nom} [14]:

$$\tan\frac{\beta}{2} + \frac{\alpha}{\beta}\left(\frac{\alpha^2 + g^2}{\beta^2 - g^2}\right)\tanh\frac{\alpha}{2} = 0 \quad (5)$$

where

$$g^2 = \omega_{\text{nom}}^2 L_r^2 \left(\frac{\rho}{E}\right) \quad (6)$$

and

$$\left.\begin{matrix}\alpha^2 \\ \beta^2\end{matrix}\right\} = \frac{g^2}{2}\left[\mp\left(1 + \frac{E}{\kappa G}\right) + \sqrt{\left(1 - \frac{E}{\kappa G}\right)^2 + \frac{4L_r^2 h W_r}{g^2 I_r}}\right]. \quad (7)$$

For comparative purposes in Section V, the Timoshenko formulation for clamped–clamped beams will also be needed. For a clamped–clamped beam with uniform cross section and without any electromechanical coupling, the equation governing the fundamental resonance frequency becomes [14]

$$\tan\frac{\beta}{2} + \frac{\beta}{\alpha}\left(\frac{\alpha^2 + g^2(\kappa G/E)}{\beta^2 - g^2(\kappa G/E)}\right)\tanh\frac{\alpha}{2} = 0. \quad (8)$$

B. Frequency Perturbations Due to Electromechanical Coupling

As stated in the above discussion, (1) and (5) constitute frequency equations for a free–free beam resonator without electromechanical coupling. To allow electrical access to its frequency characteristics, the device of Fig. 1 features an input electrode that provides capacitive electromechanical coupling when appropriate dc bias and ac excitation voltages are applied. However, because the electrode-to-resonator capacitance is a nonlinear function of beam displacement, the addition of such capacitive electromechanical coupling can also significantly perturb the resonance frequency of the device. Specifically, V_P-derived electric fields in the electrode-to-resonator capacitive gap of a vibrating beam generate a force in quadrature with the input force. The effect of this quadrature force component can be modeled by an electrical stiffness k_e, which combines with the mechanical stiffness of the beam to establish the resonance frequency of the beam in the presence of capacitive electromechanical coupling. As described in previous literature [6]–[9], the electrical stiffness k_e varies with the dc-bias voltage V_P, making the resonance frequency also a function of V_P.

Among equations for frequency versus V_P proposed in previous literature [6]–[9], the ones in [6] and [8] best match the experimental data of this paper. Of these two, the expression from [6] not only yields a slightly better match to measurements, but also greatly reduces the required computation time. For these reasons, this paper uses the expression from [6], which for convenience and later use is repeated as

$$\begin{aligned} f_o &= \frac{1}{2\pi}\zeta\sqrt{\frac{k_r(y)}{m_r(y)}} \\ &= \frac{1}{2\pi}\zeta\sqrt{\frac{k_m(y)}{m_r(y)}}\left[1 - \left\langle\frac{k_e}{k_m}\right\rangle\right]^{1/2} \\ &= \zeta f_{\text{nom}}\left[1 - \left\langle\frac{k_e}{k_m}\right\rangle\right]^{1/2} \end{aligned} \quad (9)$$

where the variable f_o now represents the resonance frequency including electromechanical coupling, and $k_r(y)$ and $m_r(y)$ are the effective stiffness (including adjustments due to external coupling) and mass [5], [6], respectively, at any location y on the μresonator beam, indicated in Fig. 3, ζ is a fitting parameter that accounts for beam topography and finite elasticity in the anchors [6], [10], [11], and $k_m(y)$ is the *mechanical* stiffness of the μresonator at location y, similar to $k_r(y)$, but this time, for the special case when $V_P = 0$ V (i.e., no electromechanical coupling) and given by

$$k_m(y) = [2\pi f_{\text{nom}}]^2 m_r(y) \quad (10)$$

where f_{nom} is the resonance frequency of the free–free beam sans electromechanical coupling, obtained from (1) or (5). In (9), $\langle k_e/k_m\rangle$ is a parameter representing the combined electrical-to-mechanical stiffness ratios integrated over the electrode width W_e, and satisfying the relation [6]

$$\left\langle\frac{k_e}{k_m}\right\rangle = \int_{L_1}^{L_2} \frac{V_P^2 \varepsilon_o W_r}{[d(y)]^3 k_m(y)}\, dy \quad (11)$$

where ε_o is the permittivity in vacuum, $d(y)$ is the electrode-to-resonator gap spacing, which varies as a function of location y along the length of the beam due to V_P-derived forces that statically deflect the simply supported (by dimples) beam (cf. Fig. 3) [6], [8], $L_1 = 0.5(L_r - W_e)$ and $L_2 = 0.5(L_r + W_e)$ for a centered electrode, and all other geometric variables are given in Figs. 1 and 3.

The location dependences of the mass $m_r(y)$ and stiffness $k_r(y)$ in the above equations derive from the velocity dependence of these quantities and, thus, are direct functions of the free–free beam's resonance mode shape, shown in Fig. 1(c). Equations for these quantities can be obtained as modifications of a previous analysis [6] and are as follows:

$$\begin{aligned} m_r(y) &= \frac{KE_{\text{tot}}}{(1/2)(v(y))^2} \\ &= \frac{\rho W_r h \int_0^{L_r} [Z_{\text{mode}}(y')]^2 (dy')}{[Z_{\text{mode}}(y)]^2} \end{aligned} \quad (12)$$

$$k_r(y) = \omega_o^2 m_r(y). \quad (13)$$

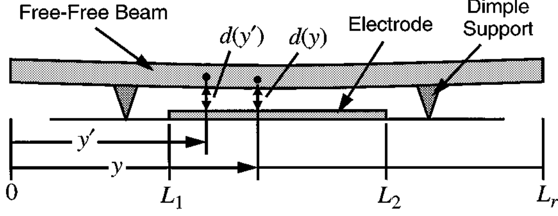

Fig. 3. Free–free beam resonator cross-sectional schematic, identifying key variables used in frequency-pulling and impedance formulations.

where $KE_{\rm tot}$ is the peak kinetic energy in the system, $v(y)$ is the velocity at location y, dimensional parameters are given in Figs. 1 and 3, and the mode shape function $Z_{\rm mode}(y)$ is

$$Z_{\rm mode}(y) = \cosh\varphi y + \cos\varphi y - \xi\left[\sinh\varphi y + \sin\varphi y\right] \quad (14)$$

where

$$\xi = \frac{\cosh\varphi L_r - \cos\varphi L_r}{\sinh\varphi L_r - \sin\varphi L_r} \quad \text{and} \quad \varphi^4 = \frac{\rho A}{EI_r}\omega_o^2 \quad (15)$$

and where ω_o is the radian resonance frequency, and I_r is the bending moment of inertia. For the fundamental mode, φL_r is 4.73. Node points are obtained by setting (14) to zero and solving for y.

C. Support Structure Design

As discussed in Section II, the free–free beam μmechanical resonator is supported by four torsional beams attached at its fundamental-mode node points, identified in Fig. 1(c) and specified via evaluation of (14) and (15). Since they are attached at node points, the support springs (ideally) sustain no translational movement during resonator vibration and, thus, support (i.e., anchor) losses due to translational movements—such as those sustained by clamped–clamped beam resonators—are greatly alleviated. Furthermore, with the recognition that the supporting torsional beams actually behave like acoustic transmission lines at the VHF frequencies of interest, torsional loss mechanisms can also be negated by strategically choosing support dimensions so that they present virtually no impedance to the free–free beam. In particular, by choosing the dimensions of a torsional support beam such that they correspond to an effective quarter-wavelength of the resonator operating frequency, the solid anchor condition on one side of the support beam is transformed to a free end condition on the other side, which connects to the resonator. In terms of impedance, the infinite acoustic impedance at the anchors is transformed to zero impedance at the resonator attachment points. As a result, the resonator effectively "sees" no supports at all and operates as if levitated above the substrate, devoid of anchors and their associated loss mechanisms.

The above transformation is perhaps more readily seen using the equivalent acoustic T network model for a torsional beam using the current analogy, where force is the across variable and velocity is the through variable [15]. In particular, when the dimensions of a given support beam correspond to an effective quarter-wavelength of the resonator operation frequency, its equivalent acoustic T network takes the form shown in Fig. 4(b), where shunt and series arm impedances are modeled by equal and opposite stiffnesses, k_b and $-k_b$. Given that in this current analogy mechanical circuit [15], anchoring the beam of Fig. 4(a) at side B corresponds to opening the B port of Fig. 4(b), it is clear by cancellation of the remaining impedances, $k_b/j\omega$ and $-k_b/j\omega$ in the circuit of Fig. 4(b), that the impedance seen at port A will be zero.

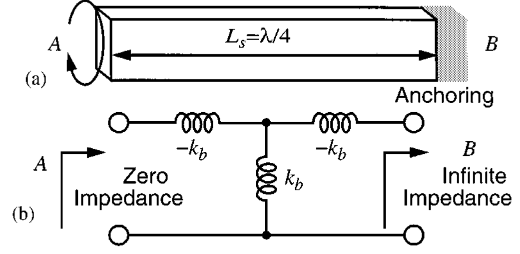

Fig. 4. (a) Quarter-wavelength torsional beam with B side anchoring. (b) Equivalent acoustic network showing zero impedance at port A with port B open.

Through appropriate acoustical network analysis, the dimensions of a torsional beam are found to correspond to a quarter-wavelength of the operating frequency when they satisfy the expression [15], [16]

$$L_s = \frac{1}{4f_o}\sqrt{\frac{G\gamma}{\rho J_s}} \quad (16)$$

where the subscript s denotes a support beam, J_s is the polar moment of inertia, given by

$$J_s = hW_s\frac{\left(h^2 + W_s^2\right)}{12} \quad (17)$$

and γ is the torsion constant [16], given for the case of a rectangular cross section with $h/W_s = 2$ by

$$\gamma = 0.229hW_s^3. \quad (18)$$

D. Transducer Design

The value of the electrical series motional resistance R_z (among other impedance elements) seen looking into the input electrode of a μmechanical resonator is of utmost importance in both filtering and oscillator applications [5], [6]. As with previous capacitively transduced clamped–clamped beam μmechanical resonators, parameters such as W_e, W_r, and d, which directly influence the electrode-to-resonator overlap capacitance, have a direct bearing on the electrical impedance seen looking into the input electrode, as does the dc-bias V_P applied to the resonator. By appropriate impedance analysis, the expression governing R_z for this capacitively transduced free–free beam μmechanical resonator takes on the form [6]

$$R_z = \frac{V_i}{I_z} = \left[\int_{L_1}^{L_2}\int_{L_1}^{L_2} \frac{\omega_o Q V_P^2 (\varepsilon_o W_r)^2}{\left[d(y')d(y)\right]^2 k_m(y')} \cdot \frac{Z_{\rm mode}(y)}{Z_{\rm mode}(y')}\, dy'\, dy\right]^{-1} \quad (19)$$

where $L_1 = 0.5(L_r - W_e)$ and $L_2 = 0.5(L_r + W_e)$ for a centered electrode.

As discussed in Section II, under normal operation, the free–free beam resonator must be pulled down onto its supporting dimples via a dc-bias voltage V_P applied to the resonator. Only when the dimples are "down" is the electrode-to-resonator gap spacing d small enough to provide

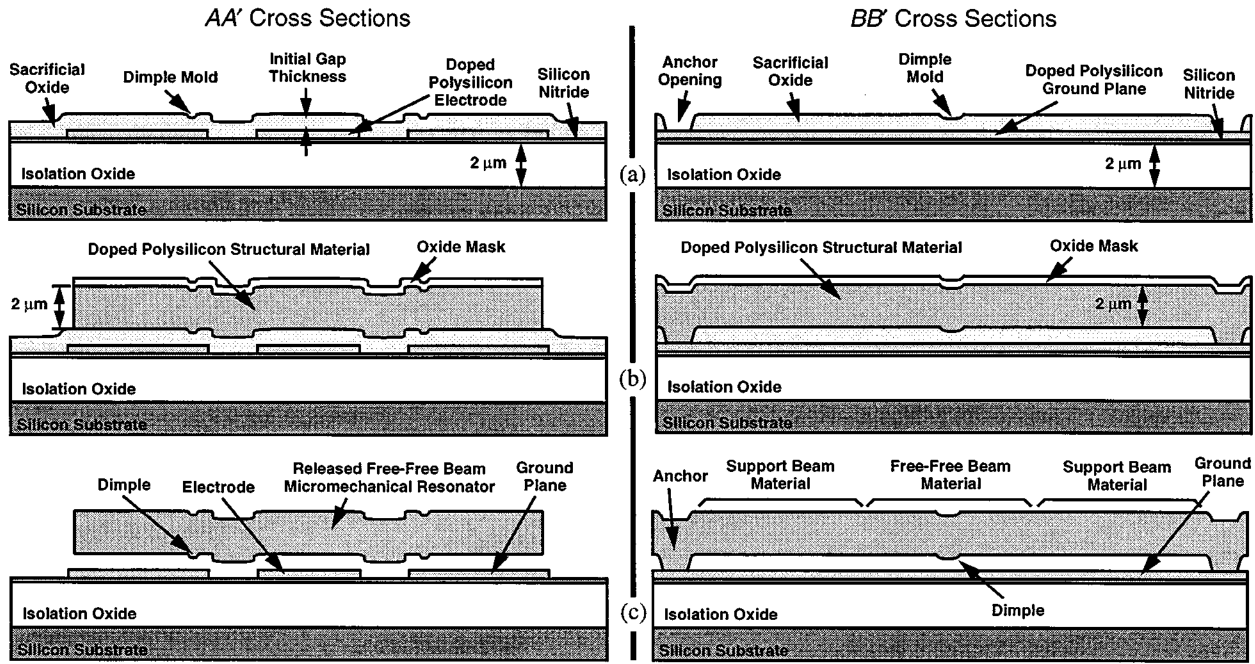

Fig. 5. Free–free μmechanical beam fabrication process flow with cross sections taken along AA' and BB' in Fig. 1. (a) Cross sections after sacrificial oxide deposition and patterning to form anchors and dimple molds. (b) Cross sections after structural polysilicon deposition and patterning. (c) Final cross sections after structural release.

adequate electromechanical coupling for most applications. Thus, when designing the device input electrode, careful consideration must be given to not only the input impedance seen when looking into the electrode, but also to the V_P required to pull the dimples down. This V_P voltage should be sufficient to pull the resonator down onto its dimples, yet small enough to avoid further pull-down of the free–free beam into the electrode after the dimples are down. Symbolically, the dc-bias voltage V_P must satisfy the relation

$$V_c > V_P > V_d \tag{20}$$

where V_d is the dimple-down voltage, and V_c is the catastrophic resonator pull-down voltage.

When pulling the resonator down onto its dimples, since the supporting beams are often much more compliant than the free–free resonator beam, very little bending occurs in the resonator itself. (In particular, for the 70-MHz design of Table I in Section V, the combined stiffness of the supporting beams is 534 N/m, which is more than 100× smaller than the 57 390 N/m at the midpoint of the free–free resonator beam.) Thus, the restoring force inhibiting pull-down is uniform over the electrode, and the expression for the dimple-down voltage V_d takes on the form [17]

$$V_d = \sqrt{\frac{8}{27}\frac{k_s d_{\text{ini}}^3}{W_r W_e}} \quad \text{where} \quad k_s = E W_s \left(\frac{h}{L_s}\right)^3 \tag{21}$$

where k_s is the combined stiffness of all the supporting beams, and d_{ini} is the initial electrode-to-resonator gap before the beam is brought down to its dimples.

Once the dimples are down, further movement of the resonator beam toward the electrode is attained via bending of the resonator itself. The electrode now sees a distributed stiffness inhibiting pull-down, which now must be integrated over the electrode area to accurately predict the catastrophic resonator pull-down voltage V_c. The procedure for determining V_c then amounts to setting (11) equal to unity and solving for the V_P variable.

IV. Fabrication

Fig. 5 summarizes the five-mask polysilicon surface-micromachining technology used to fabricate the resonator devices of this paper. The fabrication sequence begins with isolation layers formed via successive growth and deposition of 2-μm thermal oxide and 2000 Å LPCVD Si_3N_4, respectively, over a ⟨100⟩ lightly doped p-type, silicon wafer. Next, 3000 Å of LPCVD polysilicon is deposited at 585 °C and phosphorous-doped via ion implantation, then patterned to form ground planes and interconnects. An LPCVD sacrificial oxide layer is then deposited to a thickness dictated by (21), after which successive masking steps are used to achieve dimples and anchor openings [cf. Fig. 5(a)]. To insure accurate depths, dimples are defined via a precisely controlled reactive-ion etch using a CF_4 chemistry. Anchors, on the other hand, are simply wet etched in a solution of buffered hydrofluoric acid (BHF).

Next, the structural polysilicon is deposited via LPCVD at 585 °C and phosphorous dopants are introduced via ion implantation. A 2000-Å-thick oxide mask is then deposited via LPCVD at 900 °C, after which wafers are annealed for 1 h at 1000 °C to relieve stress and distribute dopants. Both the oxide mask and structural layer are then patterned via SF_6/O_2- and Cl_2-based RIE etches, respectively [cf. Fig. 5(b)], and structures are then released via a 5-min etch in 48.8 wt HF [cf. Fig. 5(c)]. Note that this release etch time is significantly shorter than that required for previous clamped–clamped beam resonators (∼1 h) that did

TABLE I
FREE–FREE BEAM DESIGN AND PERFORMANCE SUMMARY

	Row No.	Parameter	Source	Target Frequency				Unit
				30 MHz	50 MHz	70 MHz	90 MHz	
Designed/Fabricated/Given	1	Resonator Beam Length, L_r	layout	23.2	17.8	14.9	13.1	μm
	2	Resonator Beam Width, W_r	layout	10	10	6	6	μm
	3	Supporting Beam Length, L_s	layout	30.6	18.4	13.1	10.3	μm
	4	Supporting Beam Width, W_s	layout	1	1	1	1	μm
	5	Node Location 1, L_{n1}	layout	5.2	4	3.3	2.9	μm
	6	Node Location 2, L_{n2}	layout	18	13.8	11.6	10.2	μm
	7	Polysilicon Film Thickness, h	measured	2.05	2.05	2.05	2.05	μm
	8	Electrode Width, W_e	layout	7.4	4.5	4	2.8	μm
	9	Typical Initial Physical Gap, d_{ini}	measured	1,600	1,600	1,600	1,600	Å
	10	Typical Physical Dimple Height, d	measured	1,230	1,230	1,230	1,230	Å
	11	Torsion Constant, γ	Eq. (18)	0.469	0.469	0.469	0.469	μm^4
	12	Young's Modulus, E	measured	150	150	150	150	GPa
	13	Poisson Ratio, ν	[19]	0.226	0.226	0.226	0.226	—
	14	Freq. Modification Factor, ζ	chosen	1	1	1	1	—
Measured	15	Measured Frequency, f_o	measured	31.51	50.35	71.49	92.25	MHz
	16	Measured Quality Factor, Q	measured	8,110	8,430	8,250	7,450	—
	17	V_P Used in Measurement, V_{Pm}	measured	22	86	126	76	V
	18	Measured Series Resistance, R_z	meas./Eq. (24)	31.1	10.7	34.9	167.0	kΩ
Analytically Determined	19	Timoshenko Freq., $f_o(V_P{=}V_{Pm})$	Eq. (9), (5)	30.63	50.83	71.39	90.99	MHz
	20	Timoshenko Freq., $f_o(V_P{=}0V)$	Eq. (5)	30.70	51.16	71.64	91.07	MHz
	21	Euler-Bernoulli Freq., $f_o(V_P{=}V_{Pm})$	Eq. (9), (1)	31.62	53.51	76.57	99.29	MHz
	22	Euler-Bernoulli Freq., $f_o(V_P{=}0V)$	Eq. (1)	31.68	53.82	76.81	99.36	MHz
	23	Calculated Series Resistance, R_z	Eq. (19)	30.9	10.8	34.8	168.9	kΩ
	24	Adjusted/Extrapolated Gap, d	Eq. (19)	1,300	1,510	1,920	1,780	Å
	25	Resonator Stiffness, $k_r(y{=}L_r/2)$	Eq. (13)	27,423	57,926	57,390	81,965	N/m
	26	Resonator Mass, $m_r(y{=}L_r/2)$	Eq. (12)	7.40×10^{-13}	5.68×10^{-13}	2.85×10^{-13}	2.51×10^{-13}	kg
	27	Dimple-Down Voltage, V_d	Eq. (21)	9.2	25.3	57.4	98.2	V
	28	Catastrophic Pull-In Voltage, V_c	Eq. (11) = 1	232	521	1024	1262	V

not benefit from dimple-activated gap spacings and, thus, required sacrificial oxide thicknesses on the order of hundreds of angstroms [2].

After structural release, aluminum is evaporated and patterned over polysilicon interconnects via liftoff to reduce series resistance. Fig. 6 presents the scanning electron micrograph (SEM) of a prototype 71.49-MHz free–free beam flexural-mode μmechanical resonator, indicating various components and dimensions. An SEM showing the underside of this resonator (obtained via a fortunate wafer cleaving) is shown in Fig. 7, where the supporting dimples are clearly seen.

V. EXPERIMENTAL RESULTS

Several free–free beam μresonators with frequencies from 30 to 90 MHz and with varying initial gaps and dimple depths were designed using the methods detailed in Section IV, then fabricated using the process flow described above and shown in Fig. 5. In addition to free–free beam resonators, clamped–clamped versions [2], and even folded-beam, comb-transduced lateral resonators [18] were included in this run for comparative purposes. Table I summarizes design and layout data for four of the free–free beam resonators, with reference to the parameters and dimensions indicated in Fig. 1. Table II summarizes two of the clamped–clamped beam μresonators, with reference to dimensions and parameters from [6].

A custom-built vacuum chamber with printed circuit board support and electrical feedthroughs allowing coaxial and dc connections to external instrumentation was utilized to characterize all resonators. In this apparatus, devices-under-test were epoxied to a custom-built printed circuit board containing surface-mounted detection electronics, and data was collected using an HP 4195A Network/Spectrum Analyzer. A turbomolecular pump was used to evacuate the chamber to pressures on the order of 50 μtorr (which removes viscous gas damping mechanisms [20]) before testing devices.

To assess the overall quality of the structural polysilicon deposited for this paper, 416 –kHz folded-beam μmechanical resonators were tested first under 50-μtorr vacuum using a previ-

TABLE II
CLAMPED–CLAMPED BEAM DESIGN AND PERFORMANCE SUMMARY

	Row No.	Parameter	Source	Target Frequency ~50 MHz	Target Frequency ~70 MHz	Unit
Designed/Fabricated/Given	1	Resonator Beam Length, L_r	layout	16	14	μm
	2	Resonator Beam Width, W_r	layout	8	6	μm
	3	Polysilicon Film Thickness, h	measured	2.1	2.1	μm
	4	Electrode Width, W_e	layout	8	7	μm
	5	Typical Initial Physical Gap, d	measured	300	300	Å
	6	Young's Modulus, E	measured	150	150	GPa
	7	Poisson Ratio, ν	[19]	0.226	0.226	—
	8	Freq. Modification Factor, ζ	chosen	0.856	0.871	—
Measured	9	Measured Frequency, f_o	measured	54.2	71.8	MHz
	10	Measured Quality Factor, Q	measured	840	300	—
	11	V_P Used in Measurement, V_{Pm}	measured	35	28	V
	12	Measured Series Resistance, R_z	meas./Eq. (24)	8.67	35.2	kΩ
Analytically Determined	13	Timoshenko Freq., $f_o(V_P=V_{Pm})$	Eq. (9), (8)	54.27	71.94	MHz
	14	Timoshenko Freq., $f_o(V_P=0\text{V})$	Eq. (8)	55.74	73.17	MHz
	15	Euler-Bernoulli Freq., $f_o(V_P=V_{Pm})$	Eq. (9), (1)	57.01	76.47	MHz
	16	Euler-Bernoulli Freq., $f_o(V_P=0\text{V})$	Eq. (1)	58.41	77.62	MHz
	17	Calculated Series Resistance, R_z	[6]: Eq. (18)	8.48	35.9	kΩ
	18	Adjusted/Extrapolated Gap, d	[6]: Eq. (18)	700	580	Å
	19	Resonator Stiffness, $k_r(y=L_r/2)$	[6]: Eq. (9)	28,496	32,870	N/m
	20	Resonator Mass, $m_r(y=L_r/2)$	[6]: Eq. (7)	2.45×10^{-13}	1.61×10^{-13}	kg
	21	Catastrophic Pull-In Voltage, V_c	[6]: Eq. (15) = 1	108	106	V

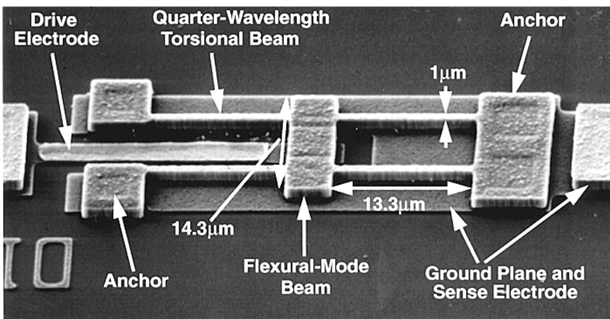

Fig. 6. SEM of a 71.49-MHz free–free beam μmechanical resonator.

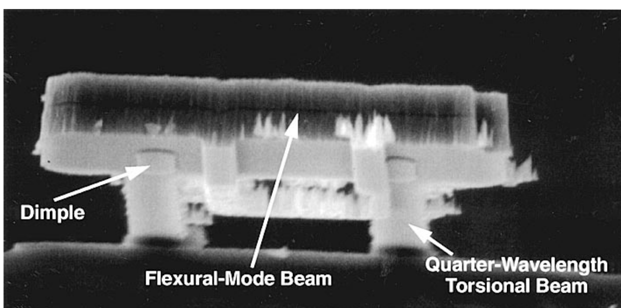

Fig. 7. Underside SEM of a free–free beam design, explicitly showing the supporting dimples.

ously described transresistance amplifier detection circuit with a gain of $R_{\rm amp} = 100\ {\rm k}\Omega$ [21], [22]. Fig. 8 presents the measured frequency characteristic for a typical one of these resonators, showing a Q of only 15 000—much lower than the 50 000 of previous runs [21], [22], indicating suboptimal polysilicon material in this particular run. Although lower than desired, this Q still proved sufficient for the present clamped–clamped versus free–free beam comparison.

For later comparison with the single-beam μmechanical resonators of this paper, it is instructive to obtain a value for the series motional resistance R_x of this resonator. Pursuant to this, we first note that the decibel value in the y-axis of Fig. 8 corresponds to the gain from the input of the test resonator to the output of the transresistance amplifier, given by

$$A = 20 \log \left| \frac{R_{\rm amp}}{Z_x} \right| \quad [\text{dB}] \tag{22}$$

where Z_x is the impedance of the resonator. Using (22) and the -33-dB peak value, shown in Fig. 8, the R_x of this folded-beam capacitive-comb-transduced μmechanical resonator is found to be 4.47 MΩ—a typical value for this type of resonator with $V_P = 50$ V [22].

Clamped–clamped beam μmechanical resonators using parallel-plate capacitive transduction were tested next, again under a pressure of 50 μtorr, but now without the transresistance amplifier, using the more direct detection scheme shown in Fig. 1, with $L_c = 100\ \mu$H, $C_\infty = 0.1\ \mu$F, and $R_L = 50\ \Omega$. Note that

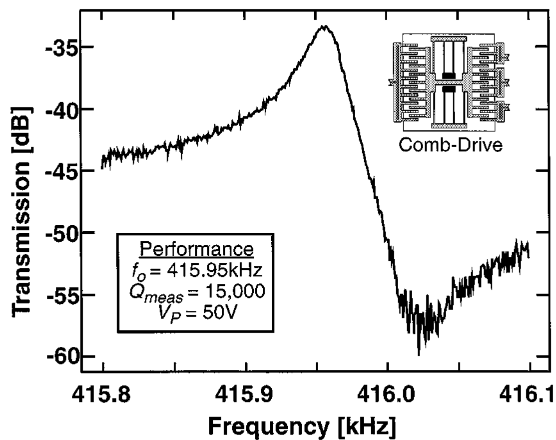

Fig. 8. Measured frequency characteristic for a 415.95-kHz folded-beam comb-driven μmechanical resonator fabricated in the run used for this paper.

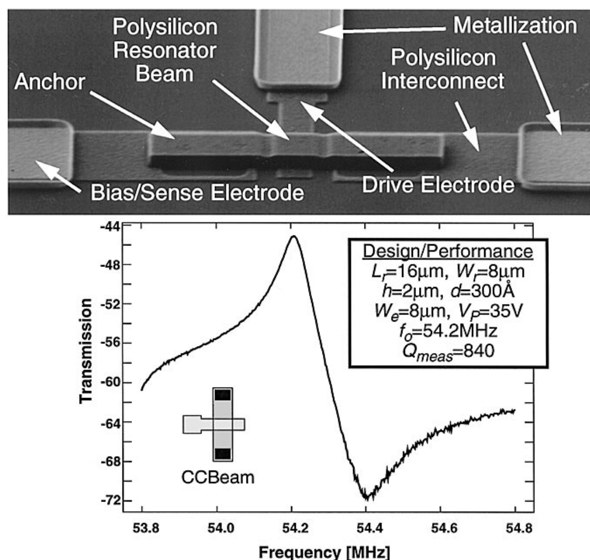

Fig. 9. SEM and measured frequency spectrum for a 54.2-MHz clamped–clamped beam μmechanical resonator.

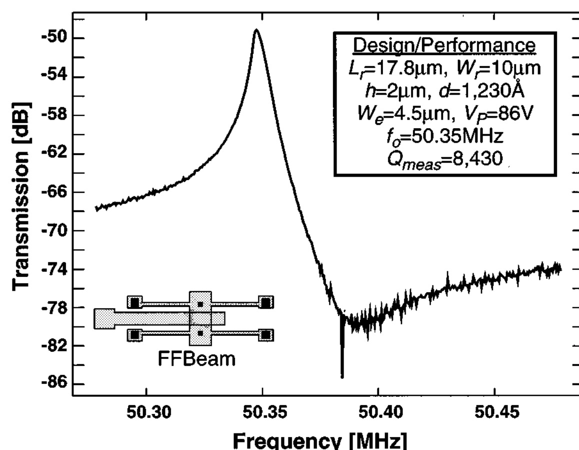

Fig. 10. Measured frequency spectrum for a 50.35-MHz free–free beam μmechanical resonator.

a transresistance amplifier is not needed for this measurement since the small-gapped parallel-plate capacitive transducers of these resonators are much stronger than the capacitive-comb transducer of the previous resonator.

Fig. 9 presents the SEM and measured frequency characteristic for a 54.2-MHz clamped–clamped beam resonator. The directly measured Q of this device, with 180 Ω of interconnect series resistance R_p included, is $Q_l = 840$. The actual unloaded Q of the device can be obtained via

$$Q = Q_l\left(1 + \frac{R_p}{R_z}\right) \tag{23}$$

where R_z can be obtained from the measured frequency spectrum to be

$$R_z = R_L(10^{-(A/20)} - 1) - R_p \tag{24}$$

where A is the transmission gain in decibels at the peak of the measured frequency characteristic. (Note that because it is determined from an impedance-mismatched single resonator circuit, and not from a properly terminated filter structure [6], A is *not* the same as insertion loss.)

Taking $A = -45$ dB, (24) yields $R_z = 8.67$ kΩ, which is orders of magnitude lower than the 4.47 MΩ seen for the previous comb-driven resonator, clearly demonstrating the advantages of thin-gap parallel-plate capacitive transducers. Equation (23) gives $Q = 858$—not much different from the measured loaded value. This will, in general, be true for all other devices of this paper, due to the conservative electrode-to-resonator gap spacings used. (Several of the effective gaps achieved in this paper are $>$1000 Å, which are conservative in comparison with, e.g., $d < 300$ Å.)

The frequency characteristic for a 50.3-MHz free–free beam μmechanical resonator was then obtained under the same pressure, using an identical circuit (but with a different V_P to accommodate electrode-to-resonator gap spacing differences). Fig. 10 presents the measured result, clearly showing a substantially higher Q, with a directly measured value of $Q_l = 8430$, and an extracted value of $Q = 8743$ when accounting for 400 Ω of interconnect series resistance loading the resonator $R_z = 10.74$ kΩ. Even greater Q discrepancies are observed in Fig. 11(a) and (b), which compares measured spectra for clamped–clamped and free–free beam μmechanical resonators around 70 MHz, showing a Q difference as large as 28× at this frequency.

Given that the devices yielding Figs. 9–11(a) and (b) differ in only their end conditions (i.e., their anchoring methods), these data strongly suggest that anchor dissipation becomes a dominant loss mechanism for clamped–clamped beam resonators with high stiffness at VHF frequencies, and that the use of free–free beam resonators with nonintrusive supports can greatly alleviate this loss mechanism.

In addition, the data in Figs. 9 and 11(a) also show that clamped–clamped beam resonators exhibit a lowering in Q as frequencies increase from 50 to 70 MHz, whereas their free–free beam counterparts maintain a fairly constant Q over this range. These results further support an anchor-derived loss model for clamped–clamped beam resonators, where the smaller the value of (L_r/h) for the beam (i.e., the higher the frequency), the larger the axial stiffness, and the larger the moments and forces exerted on the anchor supports per cycle

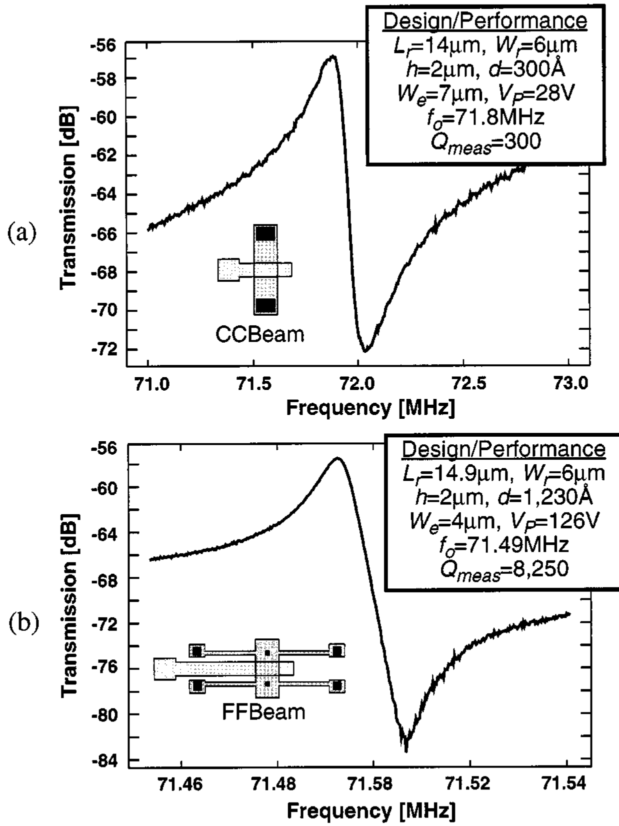

Fig. 11. Measured frequency spectra for: (a) a 71.8-MHz clamped–clamped beam μresonator and (b) a 71.49-MHz free–free beam μresonator.

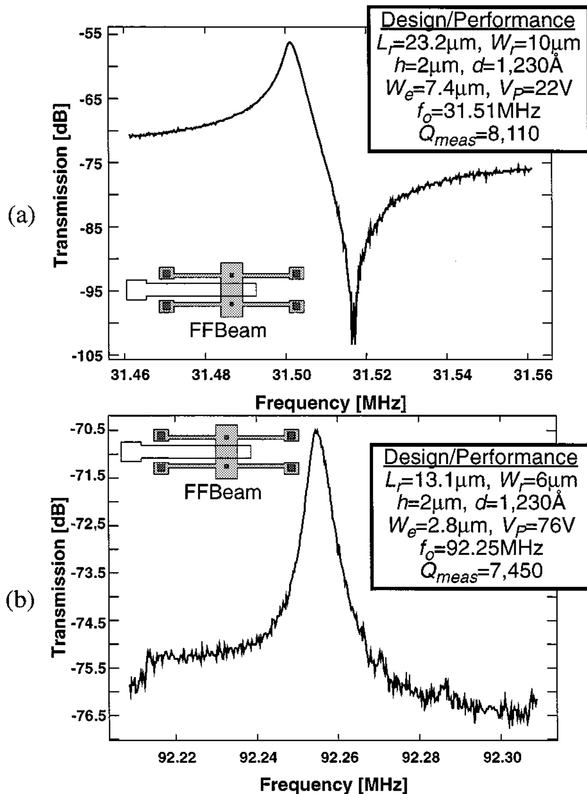

Fig. 12. Measured spectra for: (a) a 31.5-MHz free–free beam μresonator and (b) a 92.25-MHz free–free beam μresonator.

[10]. These then lead to larger deformations or displacements at the anchor supports, which, in turn, degrade the overall Q, since the Q of a clamped–clamped beam flexural-mode mechanical resonator is generally inversely proportional to the square of displacements at its anchors [23]. Under this model, the free–free beam resonators of this paper, which (ideally) have no anchors, should exhibit Qs largely independent of frequency, at least in this VHF range. In this respect, Figs. 10 and 11(b) are certainly consistent with an anchor-dominated dissipation model, as are additional data at 31.51 and 92.25 MHz, shown in Fig. 12(a) and (b), respectively.

Table I compares the free–free beam resonator data in Figs. 10–12 with theoretical predictions using the indicated analytical expressions of Section III. Table II presents similar data for the clamped–clamped beam resonators of Figs. 9 and 11(a). For the predicted values in each table, the data in the "Designed/Fabricated/Given" portion was used, except for the V_P-influenced frequency $f_o(V_P = V_{Pm})$ and the series motional resistance R_z, for which an adjusted value of electrode-to-resonator gap spacing d (row 24) was utilized to fit the calculated R_z value to measured data. This adjusted value of d is also predicted when matching measured f_o versus V_P curves with those generated by self-consistent finite-element simulators [24], and can be construed as the actual electrode-to-resonator gap spacing, which differs from the target gap spacing due to several possible factors, including the following:

1) V_P-induced depletion in the doped-silicon structure that substantially increases the effective gap spacing over the actual physical value [6];
2) uncertainty in the measured value of the sacrificial oxide spacer layer (which determines the initial gap spacing $d_{\rm ini}$ for free–free beams and the gap spacing d for clamped–clamped beams);
3) uncertainty in the depth of the dimples after the dimple etch (which determines the activated gap spacing d for free–free beams).

When comparing the magnitudes of the adjusted values for d with those of the target physical values in rows 24 and 10, respectively, of Table I, there is some question as to whether or not some of the free–free beam resonators where actually down on their dimples during measurement. Specifically, although the adjusted d's for the 30- and 50-MHz designs are close enough to 1230 Å that it is conceivable with the explanations of items 1)–3) above that these beams were down on their dimples during measurement, the measured versus adjusted d discrepancies for the 70- and 90-MHz designs seem a bit too large at first glance. For the 70-MHz resonator, the discrepancy may be explainable by recognizing that a very large dc-bias $V_P = 126$ V, was used in this measurement, perhaps inducing a larger depletion region than for other resonators. Thus, it is plausible that the 70-MHz resonator was actually down on its dimples during measurement, but had a larger effective gap than its 30- and 50-MHz counterparts due to excessive depletion.

Since a smaller V_P was used for testing, the above depletion argument may not be sufficient to explain the measured versus adjusted d discrepancy for the 90-MHz resonator. This resonator beam may, in fact, not have been down on its dimples

during measurement, especially since the $V_P = 76$ V used is less than the predicted pull-down voltage $V_d = 98$ V. Note that the dimple-down voltage in row 27 of Table I was determined using the initial gap spacing d_{ini} of row 9, while the catastrophic pull-in voltage in row 28 of Table I was calculated using the adjusted d values of row 24. As will be seen later in this section, the above uncertainties make it difficult at present to quantify the effect of the dimples on resonator performance.

At this point, some explanation for the rather large values of V_P used in the measurements of Figs. 10–12 is in order. These were required mainly because very conservative values for dimple height d and initial electrode-to-resonator gap spacing d_{ini} were used in these prototype designs (cf. Table I). With smaller values of d or d_{ini} (e.g., 300 Å), much smaller V_P's on the order of 5 V can be used [2].

A. Timoshenko Versus Euler–Bernoulli Design Methods

In addition to measured values for resonance frequency, Tables I and II also include analytical values, computed using both Timoshenko and Euler–Bernoulli methods. These data are summarized in rows 19–22 of Table I for free–free beams, and rows 13–16 of Table II for clamped–clamped beam designs. In both tables, the adjusted value of d was used to determine the effect of electromechanical coupling on frequency. (Recall that the adjusted d was determined by matching measured and calculated R_z values.) As is evident from both tables, (9)–(11) predict that V_P-induced electrical spring stiffnesses k_e generate only minor shifts in the resonance frequencies of VHF flexural-mode μmechanical resonators, on the order of only 0.3% for the 70-MHz design. This is not surprising, given the large mechanical stiffnesses of these VHF resonators and the rather conservative electrode-to-resonator gap spacings used.

Upon comparison of measured resonance frequencies in row 15 with predicted frequencies in rows 19 and 21 of Table I, the Timoshenko theory is clearly the more accurate of the two, consistently predicting frequencies within 3% of the measured value for free–free beam designs. In contrast, frequency predictions based on the Euler–Bernoulli theory get worse as frequencies increase, and are as much as 7.6% too high for the 90-MHz design. Evidently, the Timoshenko design techniques are necessary when designing 2-μm-thick 6-μm-wide flexural-mode resonators with frequencies in the upper VHF range.

As discussed earlier, the frequency modification factor ζ serves as a metric gauging the impact of surface topography and anchor effects on resonance frequency [6], [10], [11]. In general, $\zeta = 1$ when these effects are not important, and <1 otherwise. For the clamped–clamped beams of Table II, to maximize its role as a metric, ζ was chosen to match exactly the measured and Timoshenko-calculated values of rows 9 and 13. The degree to which $\zeta < 1$ for these resonators verifies an expectation that surface topography and finite anchor elasticity greatly influence the resonance frequencies of clamped–clamped beams [10], [11]. In contrast, for the free–free beams of Table I, $\zeta = 1$ was used with little impact on the matching of measured and predicted frequencies. This not only verifies an expectation that finite anchor elasticity is not an issue for free–free beam resonators, but also suggests that surface topography may not be either.

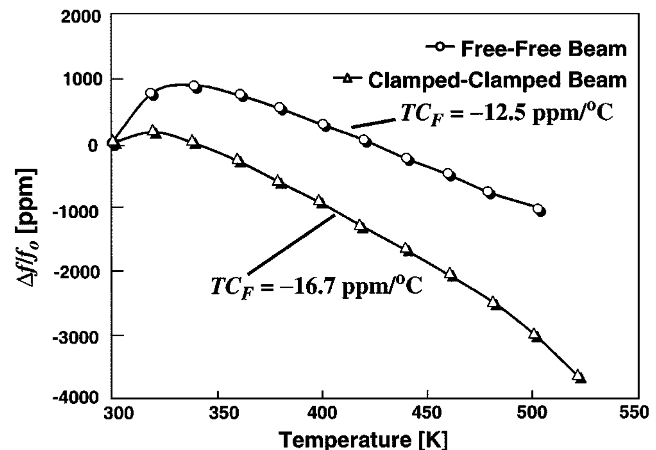

Fig. 13. Fractional frequency versus temperature plots for a clamped–clamped beam and a free–free beam μmechanical resonator.

B. Temperature Dependence

Since they are virtually levitated above the silicon substrate and, thus, should be nearly impervious to the structure-to substrate thermal expansion mismatches that plague clamped–clamped beam resonators, one might expect the described free–free beam resonators to exhibit slightly different thermal dependencies than their clamped–clamped beam counterparts. To test this assumption, modifications were made to the custom-built vacuum chamber to allow insertion of an MMR Technologies temperature-controllable cantilever, enabling measurement of the temperature dependence of resonator center frequencies under vacuum environments [25].

Fig. 13 presents measured plots of fractional frequency change versus temperature for a 53.6-MHz free–free beam μmechanical resonator and a 4.2-MHz clamped–clamped beam lateral μmechanical resonator. From the linear regions of the curves, the extracted temperature coefficients TC_F's are -12.5 ppm/°C and -16.7 ppm/°C for the free–free and clamped–clamped versions, respectively. Although the free–free beam does show slightly better performance, the degree of improvement is not large. This suggests that either the difference in thermal expansion between the silicon substrate and polysilicon resonator beam is not substantial or that the stiffnesses of these high-frequency resonators is so large—on the order of 60 000 N/m—and their lengths so small, that stiffness changes due to thermal expansion stresses are now insignificant in comparison and, thus, have less influence on the thermal stability of f_o. Whatever the reason, the smaller TC_F for the free–free beam is an indication that the polysilicon structural material in these resonators has a larger thermal expansion coefficient than that of the single-crystal silicon substrate.

Fig. 13 not only provides thermal stability information, it also elucidates an important issue concerning microscale devices: susceptibility to contamination. In particular, Fig. 13 shows peaked curves, where frequency initially rises with temperature then drops past a certain threshold temperature. This behavior can be explained by a mass-removal-based model, where contaminants that adsorb onto the resonator surfaces at low temperatures are burned or evaporated off the

resonator surfaces as temperatures increase, removing excess mass, and initially raising the frequency of the resonator. When all contaminants are removed, the frequency increase ceases, and the expected decrease in frequency with temperature (due to a negative Young's modulus temperature coefficient) is then observed. Given that typical micromechanical resonator masses are on the order of 10^{-13} kg, such a model is quite plausible, and even expected, even under the high vacuum environment used to obtain Fig. 13 [26], [27]. Admittedly, however, the vacuum achieved in our custom chamber may have lacked sufficient purity, especially given out-gassing from inserted circuit boards. For this reason, vacuum encapsulation at the wafer or package level is being investigated as a means to alleviate the observed contamination phenomena.

C. Spurious Responses

Although very effective for maximizing the Q of μmechanical resonators, the described free–free beam design may exhibit one important drawback in that its more complex design may lead to spurious modes. For example, a trampo-line mode, where the support beams all flex in unison and the entire resonator and support-beam structure vibrates in a direction perpendicular to the substrate, is possible if the dimples are not held strongly to the substrate by the applied V_p. Such modes, if not suppressed or moved to distant frequencies, can interfere with the performance of filters or oscillators utilizing this resonator design. Fig. 14 presents the frequency characteristic for a 55-MHz free–free beam μmechanical resonator measured over a wide frequency range, i.e., from 1 kHz to 100 MHz, in search of spurious modes. One spurious peak is observed at 1.7 MHz, which is sufficiently far from the desired frequency (55 MHz) to be rendered insignificant for many applications. Note that there is no conclusive evidence that this peak actually denotes a spurious mechanical mode; it may, in fact, be merely a spurious electrically resonant artifact in the measurement setup. If, however, it did represent a spurious mode, and if it was not sufficiently far from the desired resonance peak, modifications to the supports can be made to move this peak even further away, or damping strategies based on low-Q filtering or support material modifications can be used to remove the peak entirely [15].

It should be mentioned that a rather excessive amount of parasitic feedthrough is observed in the wide range measurement of Fig. 14, and this feedthrough becomes especially troublesome past 90 MHz. Shielding measures at both the board and substrate levels are planned to alleviate this feedthrough component for future measurement of even higher frequency resonators.

D. Impact of Dimples on Q

Although the dimples in this design are centered at transverse nodal locations along the length of the free–free beam, their finite widths prevent them from acting as true nodal supports. In particular, frictional losses are still possible if the edges of finite-width dimples are allowed to rub the along the substrate surface during resonance vibration. The amount of loss and, thus, the Q of a given resonator, is expected to depend upon how strongly or loosely the dimples are held down onto the substrate.

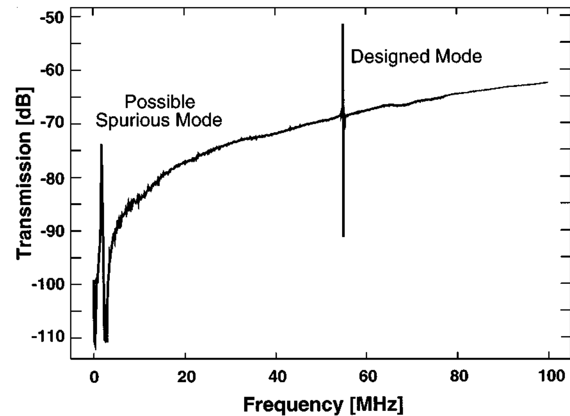

Fig. 14. Frequency characteristic for a 55-MHz free–free beam μmechanical resonator measured over a wide frequency range in search of spurious responses.

Unfortunately, as described earlier in this section, there is some question as to whether or not the dimples were even down during the measurements of Figs. 10–12. In addition, Q versus V_P data were inconclusive on this matter. In particular, for some resonators, increases in V_P led to decreases in Q, possibly indicating that added pressure on the dimples leads to an increase in radiated energy into the substrate via friction. However, an equal number of resonators showed Q increases with increasing V_P, indicating the exact opposite. With these conflicting observations, and with the knowledge that the Q of capacitively transduced μmechanical resonators seems to depend on V_P regardless of the presence of dimples [28], [29], there is insufficient data at present on which to evaluate the impact on Q of the dimple-defined gap feature of this design. Further investigations on this topic are in progress.

VI. Conclusions

Using a combination of quarter-wavelength torsional supports attached at node points and an electrically activated dimple-determined electrode-to-resonator gap, the free–free beam μmechanical resonator design demonstrated in this paper adeptly removes the anchor dissipation and processing problems that presently hinder its clamped–clamped beam counterparts and, in doing so, successfully extends the application range of high-Q microelectromechanical systems (MEMS) to the mid-VHF range, with plenty of Q to spare en route to even higher frequencies. The present μmechanical resonator design achieves Qs exceeding 8000 in a frequency range that includes some of the most popular IFs used in many cellular and cordless communication transceivers, and does so while retaining the high stiffness needed to maintain adequate dynamic range in both oscillator and filtering applications.

The VHF frequencies demonstrated in this paper by no means represent the ultimate range of μmechanical resonator technology, especially given that the observed Q of this design

seems to maintain its high value throughout the designed range of frequencies, showing little or no rolloff with increasing frequency. Needless to say, research toward UHF and beyond continues.

ACKNOWLEDGMENT

The authors are grateful for the fabrication support from Q. Bai, and testing support from Y. Yu, and H. Ding, all former graduate student researchers at The University of Michigan at Ann Arbor, who both measured the 71.8-MHz clamped–clamped μbeam spectrum).

REFERENCES

[1] C. T.-C. Nguyen, "Micromachining technologies for miniaturized communication devices," in *Proc. SPIE*, Santa Clara, CA, Sept. 20–22, 1998, pp. 24–38.
[2] A.-C. Wong, J. R. Clark, and C. T.-C. Nguyen, "Anneal-activated, tunable, 68 MHz micromechanical filters," in *10th Int. Solid-State Sens. Actuators Conf. Tech. Dig.*, Sendai, Japan, June 7–10, 1999, pp. 1390–1393.
[3] A. N. Cleland and M. L. Roukes, "Fabrication of high frequency nanometer scale mechanical resonators from bulk Si crystals," *Appl. Phys. Lett.*, vol. 69, no. 18, pp. 2653–2655, Oct. 1996.
[4] A.-C. Wong, H. Ding, and C. T.-C. Nguyen, "Micromechanical mixer+filters," in *IEEE Int. Electron Devices Meeting Tech. Dig.*. San Francisco, CA, Dec. 6–9, 1998, pp. 471–474.
[5] C. T.-C. Nguyen, "Frequency-selective MEMS for miniaturized low-power communication devices (invited)," *IEEE Trans. Microwave Theory Tech.*, vol. 47, pp. 1486–1503, Aug. 1999.
[6] F. D. Bannon, III, J. R. Clark, and C. T.-C. Nguyen, "High frequency micromechanical filters," *IEEE J. Solid-State Circuits*, vol. 35, pp. 512–526, Apr. 2000.
[7] R. T. Howe and R. S. Muller, "Resonant microbridge vapor sensor," *IEEE Trans. Electron Devices*, vol. ED-33, pp. 499–506, Apr. 1986.
[8] H. A. C. Tilmans and R. Legtenberg, "Electrostatically driven vacuum-encapsulated polysilicon resonators: Part II. Theory and performance," *Sens. Actuators A, Phys.*, vol. A45, pp. 67–84, 1994.
[9] M. W. Putty, S. C. Chang, R. T. Howe, A. L. Robinson, and K. D. Wise, "One-port active polysilicon resonant microstructures," in *Proc. IEEE Microelectromech. Syst. Workshop Dig.*, Salt Lake City, UT, Feb. 20–22, 1989, pp. 60–65.
[10] S. Bouwstra and B. Geijselaers, "On the resonance frequencies of microbridges," in *6th Int. Solid-State Sens. Actuators Conf. Tech. Dig.*, San Francisco, CA, June 24–27, 1991, pp. 538–542.
[11] Q. Meng, M. Mehregany, and R. L. Mullen, "Theoretical modeling of microfabricated beams with elastically restrained supports," *J. Microelectromech. Syst.*, vol. 2, pp. 128–137, Sept. 1993.
[12] W. T. Thomson, *Theory of Vibration with Applications*. Englewood Cliffs, NJ: Prentice-Hall, 1981.
[13] W. Weaver, Jr., S. P. Timoshenko, and D. H. Young, *Vibration Problems in Engineering*, 5th ed. New York: Wiley, 1990.
[14] W. Flugge, *Handbook of Engineering Mechanics*. New York: McGraw-Hill, 1962.
[15] R. A. Johnson, *Mechanical Filters in Electronics*. New York: Wiley, 1983.
[16] S. Timoshenko, *Strength of Materials, Part I: Elementary Theory and Problems*, 3rd ed. Melbourne, FL: Krieger, 1958.
[17] H. Nathanson, W. E. Newell, R. A. Wickstrom, and J. R. Davis, Jr., "The resonant gate transistor," *IEEE Trans. Electron Devices*, vol. ED-14, pp. 117–133, Mar. 1967.
[18] W. C. Tang, T.-C. H. Nguyen, and R. T. Howe, "Laterally driven polysilicon resonant microstructures," *Sens. Actuators*, vol. 20, pp. 25–32, 1989.
[19] H. Guckel, D. W. Burns, H. A. C. Tilmans, D. W. DeRoo, and C. Rutigliano, "The mechanical properties of fine-grained polysilicon: The repeatability issue," in *IEEE Solid-State Sens. Actuator Workshop Tech. Dig.*, Hilton Head, SC, June 1988, pp. 96–99.
[20] W. E. Newell, "Miniaturization of tuning forks," *Science*, vol. 161, pp. 1320–1326, Sept. 1968.
[21] C. T.-C. Nguyen and R. T. Howe, "An integrated CMOS micromechanical resonator high-Q oscillator," *IEEE J. Solid-State Circuits*, vol. 34, pp. 440–445, Apr. 1999.
[22] K. Wang and C. T.-C. Nguyen, "High-order medium frequency micromechanical electronic filters," *J. Microelectromech. Syst.*, vol. 8, pp. 534–557, Dec. 1999.
[23] Y. Tomikawa, S. Oyama, and M. Konno, "A quartz crystal tuning fork with modified basewidth for a high quality factor: Finite element analysis and experiments," *IEEE Trans. Sonics Ultrason.*, vol. SU-29, pp. 217–223, July 1982.
[24] V. L. Rabinovich, M. Deshpande, J. R. Gilbert, M.-A. Getillat, N. de Rooij, J. R. Clark, and C. T.-C. Nguyen, "Prediction of mode frequency shifts due to electrostatic bias," in *10th Int Solid-State Sens. Actuators Conf. Tech. Dig.*, Sendai, Japan, June 7–10, 1999, pp. 442–445.
[25] W.-T. Hsu and C. T.-C. Nguyen, "Geometric stress compensation for enhanced thermal stability in micromechanical resonators," in *Proc. IEEE Int. Ultrason. Symp. Dig.*, Sendai, Japan, Oct. 5–8, 1998, pp. 945–948.
[26] C. T.-C. Nguyen and R. T. Howe, "Design and performance of monolithic CMOS micromechanical resonator oscillators," in *Proc. IEEE Int. Freq. Control Symp. Dig.*, Boston, MA, May 31–June 3, 1994, pp. 127–134.
[27] J. R. Vig and Y. Kim, "Noise in microelectromechanical system resonators," *IEEE Trans. Utrason. Ferroelect. Freq. Contr.*, vol. 46, pp. 1558–1565, Nov. 1999.
[28] T. D. Stowe, T. W. Kenny, D. Rugar, and D. Thomson, "Dissipation microscopy based on electronic drag," in *10th Int. Solid-State Sens. Actuators Conf. Tech. Dig.*, Sendai, Japan, June 7–10, 1999, pp. 1208–1211.
[29] J. D. Zook, W. R. Herb, Y. C. Ahn, and H. Guckel, "Polysilicon sealed vacuum cavities for MEMS," in *45th Int. Vacuum, Thin Films, Processing Symp. Abstracts*, Nov. 2–6, 1998, p. 23.

Kun Wang (S'96–M'99) received the B. S. degree in electrical engineering from the University of Electronic Science and Technology of China, Chengdu, China, in 1982, and the M.S. and Ph.D. degrees in electrical engineering from The University of Michigan at Ann Arbor, in 1994 and 1999, respectively.

From 1982 to 1991, he was a Research Engineer with the Nanjing Electronic Devices Institute, Nanjing, China, where he was involved in the development of highly sensitive night-vision silicon imagers and thin-film transistors for active matrix liquid crystal displays. From 1992 to 1999, he was a Graduate Research Assistant in the Solid-State Electronics Laboratory, The University of Michigan at Ann Arbor, where he was initially involved with the growth and characterization of wide-bandgap semiconductors (GaN and AlN), and then on microelectromechanical signal processors for wireless communication applications. Since 1999, he has been with Delphi Research Laboratory, Delphi Automotive Systems, Warren, MI, as a Senior Research Engineer. His current interests include sensors and systems, and integrated-circuit design and technologies.

Ark-Chew Wong (S'91) received the B.S.E.E. and M.S.E.E. degrees from The Johns Hopkins University, Baltimore, MD, in 1994 and 1995, respectively, and is currently working toward the Ph.D. degree at The University of Michigan at Ann Arbor.

From 1994 to 1995, he was an Intern with Austria Micro System, where he was involved with testing and characterizing analog-to-digital converters (ADCs), digital-to-analog converters (DACs), and interface circuitry. His research interests include mixed-signal integrated-circuit design, MEMS for wireless communications, and other microfabrication technologies.

Mr. Wong is a member of Tau Beta Phi and Eta Kappa Nu. He was the recipient of the Best Student Paper Award presented at the 1998 International Electron Devices Meeting (IEDM).

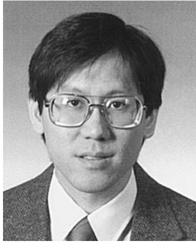

Clark T.-C. Nguyen (S'90–M'93) received the B.S., M.S., and Ph.D. degrees from the University of California at Berkeley, in 1989, 1991, and 1994, respectively, all in electrical engineering and computer sciences.

In 1995, he joined the faculty of The University of Michigan at Ann Arbor, where he is currently an Assistant Professor in the Department of Electrical Engineering and Computer Science. From 1995 to 1997, he was a member of the National Aeronautics and Space Administration's (NASA) New Millennium Integrated Product Development Team on Communications, which road-mapped future communications technologies for NASA use into the turn of the century. His research interests focus upon MEMS and include integrated micromechanical signal processors and sensors, merged circuit/micromechanical technologies, RF communication architectures, and integrated circuit design and technology.

Prof. Nguyen recently co-chaired the Workshop on Microelectromechanical Devices for RF Systems at the 1999 IEEE MTT-S Symposium. He was the recipient of the 1938E Award for Research and Teaching Excellence presented by The University of Michigan at Ann Arbor in 1998, an Electrical Engineering and Computer Science Departmental Achievement Award in 1999, and the Ruth and Joel Spira Award for Teaching Excellence in 2000. Together with his students, he received the Roger A. Haken Best Student Paper Award presented at the 1998 IEEE International Electron Devices Meeting, and the Judges Award for Best Paper at the 1998 IEEE Microwave Theory and Techniques Society (IEEE MTT-S) International Microwave Symposium.